

PLY thickness and fibre orientation effects in multidirectional composite laminates subjected to combined tension/compression and shear

Tobias Laux, Khong Wui Gan, Janice M. Dulieu-Barton, Ole T. Thomsen

PII: S1359-835X(20)30102-0
DOI: <https://doi.org/10.1016/j.compositesa.2020.105864>
Reference: JCOMA 105864

To appear in: *Composites: Part A*

Received Date: 7 November 2019
Revised Date: 13 February 2020
Accepted Date: 3 March 2020

Please cite this article as: Laux, T., Wui Gan, K., Dulieu-Barton, J.M., Thomsen, O.T., PLY thickness and fibre orientation effects in multidirectional composite laminates subjected to combined tension/compression and shear, *Composites: Part A* (2020), doi: <https://doi.org/10.1016/j.compositesa.2020.105864>

This is a PDF file of an article that has undergone enhancements after acceptance, such as the addition of a cover page and metadata, and formatting for readability, but it is not yet the definitive version of record. This version will undergo additional copyediting, typesetting and review before it is published in its final form, but we are providing this version to give early visibility of the article. Please note that, during the production process, errors may be discovered which could affect the content, and all legal disclaimers that apply to the journal pertain.



Ply thickness and fibre orientation effects in multidirectional composite laminates subjected to combined tension/compression and shear

Tobias Laux ^{a,*}, Khong Wui Gan ^{a,b}, Janice M. Dulieu-Barton ^c, Ole T. Thomsen ^c

^a School of Engineering, University of Southampton, Highfield, SO17 1BJ, Southampton, UK

^b School of Engineering, University of Southampton Malaysia, Kota Ilmu Educity @ Iskandar,
79200 Iskandar Puteri, Johor, Malaysia

^c University of Bristol, Bristol Composites Institute (ACCIS), Bristol, BS8 1TR, UK

[*t.laux@soton.ac.uk](mailto:t.laux@soton.ac.uk)

Keywords: A. Laminates, B. Strength, B. Lay-up effects, D. Mechanical testing

Abstract

The effects of laminate lay-up and multiaxial loading on the failure of multidirectional laminates can be significant. Thus, ply thickness and fibre orientation effects in quasi-isotropic carbon/epoxy laminates subjected to combined tension-shear and compression-shear loading are investigated. Three laminate lay-ups with equivalent thickness and homogenised elastic properties, but with different ply thicknesses and ply orientation angles were studied using open-hole specimens. Combined tension/compression-shear loading was applied using a new Modified Arcan Fixture (MAF). A methodology for identifying the failure behaviour based on stereo Digital Image Correlation (DIC) is devised. The results showed that ply thickness has a strong effect on the failure behaviour in combined tension-shear, whereas the effect is small in compression-shear loading. No significant effect of the relative fibre orientation angles was observed under either loading regime. The experimental approach provides a new tool to investigate composite laminates under the full tension/compression-shear loading regime.

1 Introduction

Multidirectional composite laminates made from unidirectional (UD) carbon fibre reinforced polymers are widely used in the design of lightweight structures. Their failure modes and strengths depend on the UD material system, the laminate lay-up, the stress state and any stress raisers that might be present [1]. In the present paper, the effect of laminate lay-up, i.e. ply thickness and fibre orientation, on the multiaxial open-hole specimen strength and failure behaviour in combined tension-shear and compression-shear loading is studied experimentally using a new Modified Arcan Fixture (MAF) in combination with Digital Image Correlation (DIC).

Experimental studies have shown that the laminate lay-up significantly effects failure modes and ultimate strength of composite laminates. For cross ply laminates loaded in uniaxial tension, Parvizi et al. [2] showed that the transverse tensile strength of a UD ply constrained by plies of different fibre orientations is greater than the strength of the ply in a UD laminate stack, and further that the ‘in-situ’ strength depends on the thickness of the embedded ply. Further studies have shown that the in-situ effect is not only dependent on ply thickness but also on the orientation of the constraining plies (relative angle between the plies) [3], and that the shear [4], the transverse compressive strengths [5] and delamination onset stresses [6] are all in-situ properties as well, i.e. they depend on the thickness and orientation of the constraining plies. Dvorak and Laws [7] and Camanho et al. [8] explained the physics of the in-situ effect using a fracture mechanics approach and proposed in-situ strength formulations to be used in strength based failure criteria.

Green et al. [9],[10] conducted open-hole uniaxial tension tests on a family of quasi-isotropic carbon/epoxy laminates where a different number, n , of UD plies of the same fibre orientation were blocked together, i.e. $([45_n/90_n/-45_n/0_n]_s)$, or where sub laminates were stacked together instead of blocked UD plies in a $[45/90/-45/0]_{ns}$ configuration. Specimens with single plies of each orientation dispersed through the laminate thickness failed in a brittle or fibre pull-out failure, while their open-hole strength decreased with hole size. On the other hand, it was shown

that ultimate failure of specimens with thick blocks of UD plies was governed by delamination and that the open-hole tensile strength was greater with increasing hole size [11].

Multiaxial loading also affects the failure behaviour of fibre reinforced polymer composites [12]. Most multiaxial experimental data in the open literature has been acquired using tubular test specimens [10],[11],[12] subjected to a combination of axial tension/compression, torsion and/or internal/external pressure loading. Although a wide range of multiaxial stress states can be investigated, tubular specimens do not represent most composites structures well, as these are typically flat or only slightly curved. Other approaches for multiaxial testing of flat and laminated specimens, often utilise two-actuator biaxial testing machines to subject laminates to a subset of multiaxial load cases, i.e. to combined tension-tension, compression-compression or tension-compression loading [13],[14],[15],[16],[17]. Furthermore, for testing in tension-shear [18] and compression-shear [19],[20] loading, modified versions of the original Arcan fixture [21] have been used.

Recognising that both laminate lay-up and multiaxial loading influences the open-hole specimen strength of fibre reinforced polymers, Tan et. al. [22], studied the multiaxial open-hole specimen strength of four different carbon/epoxy laminates (quasi-isotropic, 0° dominated, $\pm 45^\circ$ dominated, cross-ply) subjected to combined tension-shear and uniaxial compression. It was shown that the failure modes as well as the open-hole specimen strength in tension-shear loading are both significantly dependent on laminate lay-up as well as the multiaxial load case applied. However, combined compression-shear load cases were not investigated.

The preceding literature review [2]-[22] has shown that laminate lay-up significantly effects the strength and failure modes of multidirectional laminates. Further, it was shown that multiaxial loading alters the failure modes and open-hole specimen strengths. However, multiaxial experimental data is rarely reported in the open literature. In particular laminate lay-up effects under multiaxial loading, especially in the compression-shear loading regime, require further investigation. Thus, the aim of the research presented in the paper is to address the clear gap in the literature by experimentally assessing laminate lay-up effects in multidirectional laminates subjected to combined tension-shear and compression-shear loading. Therefore, three

quasi-isotropic laminates with different laminate lay-ups, as shown in Fig. 1, are studied.

Laminates 1 and 2 are made from UD plies with different thickness (i.e. 0.291 and 0.144 mm respectively), while Laminates 2 and 3 feature different relative fibre orientation angles (i.e. 45° and 22.5° respectively). However, all three laminates exhibit the same overall laminate thickness and equivalent homogenised elastic stiffness properties according to Classical Lamination Theory (CLT) [23].

To enable the investigation of the full combined tension/compression and shear load envelope to failure, a new Modified Arcan Fixture (MAF) is developed. In combination with the MAF, stereo DIC is used to identify initial failure and damage evolution in open-hole specimens based on the full field displacement and strains. Furthermore, DIC is used as a biaxial extensometer to derive decoupled normal and shear load-extension curves from the specimens loaded in the MAF. Based on the DIC strain maps and the load displacement curves, failure envelopes are constructed and used to assess the failure behaviour and multiaxial open-hole specimen strength. The results from the three tested laminates, enable a comparative assessment of the effects of ply thickness and fibre orientation on the failure behaviour of quasi-isotropic laminates.

The results obtained from the experimental investigation described in the paper contribute significantly to understanding the effects of laminate lay-up for multiaxial loading regimes. Furthermore, the full-field experimental data provides a challenging high-fidelity means of validating composite damage and failure modelling frameworks. The modelling frameworks described in [24],[10],[25],[26],[27],[28],[29] have shown promising capabilities in predicting the open-hole specimen strengths of laminates subjected uniaxial tension and compression but they are not sufficiently validated in multiaxial load cases. The experimental procedures described in this paper have the potential to enable more comprehensive model validations based on more challenging and thus valuable high-fidelity experimental data for multidirectional laminates subjected to multiaxial loading conditions.

2 Design of new MAF and experimental set-up

The development of a Modified Arcan Fixture (MAF), based on the original Arcan's fixture [21], was described in [30],[19]. The original Arcan fixture is limited to testing composite materials loaded in shear with superimposed tension or moderate compression loads. The MAF overcomes this limitation by the addition of anti-buckling rails which stabilise the rig against out-of-plane displacements when compressive loading is applied, thus enabling unlimited testing of specimens subjected to tension, compression, shear, combined tension/shear and combined compression/shear loadings. Gan et al. used the MAF in [19] to characterise composite laminates. However, the rig was limited to testing low strength laminates ([90], [+/- 60]) exhibiting low energy matrix driven ultimate failure modes. Strong laminates with high energy delamination or fibre driven ultimate failure modes could not be investigated due to specimen slippage in the grips leading to premature bolt shear out failure at the specimen tabs. Therefore, to test the laminates proposed in Fig. 1, a new MAF design was needed. Fig. 2 provides an overview of the new MAF, which is similar in concept to the previous version of the MAF in [19],[20], but with important key design alterations that allow larger loads to be applied for general composite materials testing. Premature failure of the specimens at the grips was successfully eliminated by upsizing the clamping bolt diameters (from M6 to M12) to induce greater clamping and thus friction forces to delay specimen slippage. Furthermore, the clamping bolts were positioned outside of the specimen tabs as shown in Fig. 2 (b) to eliminate premature shear out failure at the bolt holes.

The new MAF as shown in Fig. 2 (a) consists of two boomerang shaped arms with loading holes positioned at increments of 15° , the anti-buckling rail assembly, the top and bottom connector assemblies, the grip attachment bolts, and the friction grips shown in detail in Fig. 2 (b). By connecting the new MAF via the connector assemblies to a tensile test machine as shown in Fig. 3, using the different pairs of loading holes designated by the loading angle, α , different combined tension/compression-shear stress states can be induced in the specimen, ranging from tension ($\alpha = 0^\circ$) to tension-shear ($\alpha = 15^\circ - 75^\circ$), to shear ($\alpha = 90^\circ$), to compression-shear ($\alpha = 105^\circ - 165^\circ$) and to compression ($\alpha = 180^\circ$).

The MAF arms are made from 40 mm thick high strength aluminium alloy Alumec 89. The top and bottom connector assemblies consist of two pin joint lugs made from P20 tool steel, two 24 mm diameter shoulder bolts and a M20 threaded steel rod. The connectors allow the MAF to freely rotate in both the xy - (in-plane) and yz - (transverse) planes due to the two integrated shoulder bolts per plane. This ensures that the rig and specimen are free from out-of-plane constraints, potentially arising from test machine misalignment, which may induce spurious out-of-plane bending stresses/strains in the specimen. The grips are connected to the arms via the three 24 mm diameter grip attachment bolts made from stainless steel 17-4HP-A. The knurled friction grips are made from stainless steel 17-4PH-H900, hardened to Rockwell hardness C 45 to increase their durability in contact with the specimen. The knurls are 2 mm high pyramids with square bases. The four M12 bolts per grip, shown in Fig. 2 (b), generate the required apparent friction force by applying allowable torques up to 150 Nm. Out-of-plane displacements are prevented by an anti-buckling rail assembly similar to the one used for the previous MAF in [19]. All parts were designed to withstand a safe working load of 100 kN with a factor of safety against yielding of 1.5. The arms, grips, grip attachment bolts and the connector lugs were dimensioned using detailed Finite Element analyses. The threaded connector rod and the M12 clamping bolts were dimensioned analytically according to the tensile strength requirement in [31], and the minimum thread engagement length requirement in [31],[32], whereas the shoulder bolts were dimensioned according to [33].

Two pulleys were suspended from the test machine crosshead and attached to the MAF arms to facilitate changing the loading angle α to set up different combined loading states as defined in Fig. 2 (a). Further, a balance weight system (highlighted in green in Fig. 3) was installed to counteract the moment generated by the weight of the two MAF assembly halves (17 kg per combined arm and grip assembly), which otherwise would induce additional in-plane bending stress/strains into the specimen.

Stereo DIC was used for the assessment of the full-field deformation of the specimens, where u is the horizontal, v the vertical and w the out-of-plane displacement, respectively. The strain state (vertical ε_{yy} and horizontal ε_{xx} normal strains and shear strain γ_{yx}) was derived by the

DIC software in terms of the logarithmic strain tensor. The full field deformation data was used to assess the load response of the specimens as well as to identify the initial failure sites and subsequent damage evolution. The stereo DIC system was positioned approximately 500 mm away from the specimen's front side and was realigned and calibrated for each combined load case such that the camera xy - coordinate system corresponded with the principal axes of the undeformed specimen. Camera 1 was thereby always aligned perpendicular to the specimen surface whereas Camera 2 was positioned at an angle of approximately 20° . The DIC system specifications are listed in Table 1.

To perform the DIC, the specimens were spray painted with white speckles on a black background. Using a black instead of a white background requires less paint to be applied to the already black carbon/epoxy specimens, thus resulting in a thinner layer of spray paint on the surface of the specimens. Five static images were taken before each test, which were averaged and used as the first image in the image sequence of the loaded specimen to reduce the influence of camera noise on the displacement and strain measurements. To spatially resolve the small diameter hole, a small step size of 10 pixels was selected. To select an appropriate subset size, the first image of the loaded image sequence was correlated against the averaged static image using subset sizes of 21, 31, 51 and 71 pixels. The reported noise floors were then determined as the standard deviation of the correlated static displacement and strain fields [34]. At a subset size of 51 pixels, the critical noise in the strain fields was reduced to the commonly adopted acceptable level of approximately $100 \mu\epsilon$. A subset size of 51 pixels and a step size of 10 pixels were therefore chosen for the analysis.

3 Specimen design and manufacturing

Plates were laminated according to the lay-ups in Fig. 1 using an out-of-autoclave UD carbon/epoxy prepreg system. The laminate lay-ups were selected so that ply thickness and fibre orientation effects could be investigated. To this purpose Laminate 1 consists of 8 'thick' plies, whereas Laminates 2 and 3 consist of 16 'thin' plies, where the 'thin' plies are approximately half the thickness of the 'thick' plies. The plies in Laminates 1 and 2 are orientated at the

standard quasi-isotropic fibre orientation angles, 0° , 90° and $\pm 45^\circ$, so that any differences in their failure behaviour can be related to the effect of ply thickness ($t_{\text{ply}} = 0.291 \text{ mm}$ versus $t_{\text{ply}} = 0.144 \text{ mm}$). To study the effect of the relative ply orientation angle, also referred to as the pitch angle, Laminate 3 features more dispersed fibre orientation angles with the addition of the non-standard fibre angles, $\pm 22.5^\circ$ and $\pm 67.5^\circ$. As Laminate 2 and 3 have the same ply thicknesses, differences in their failure behaviour and multiaxial strengths can be attributed to the relative fibre orientation angle (45° versus 22.5°).

The nature of damage initiation and evolution in multidirectional laminates makes the identification of an ideal specimen design for multiaxial testing challenging. The severity of stress concentrations and their locations are influenced by the combined load case, while the initial failure modes, strengths and the evolution of damage is strongly dependent on the laminate lay-up. Therefore, it is difficult to find a specimen shape which enables the comparative assessment of the failure loads across all laminate lay-ups and load cases investigated in this work. The specimen shape should promote failure at an observable location within the gauge section away from the tabs in all lay-ups (see Fig. 1) and loading configurations. A way of increasing the chance of failure initiation at a preferable location regardless of laminate lay-up and load case is the use of an artificial stress raiser such as a small hole in the gauge of the specimen [35]. Apart from the work in [18], [22], where straight-sided open-hole specimens were used for combined tension-shear testing, there are no guidelines on an ideal open-hole specimen design used with an Arcan fixture for combined tension/compression-shear testing of multidirectional laminates.

A preliminary stress/strain and failure analysis has therefore been conducted using the commercial finite element (FE) code Abaqus 6.14 [36] to study the effect of specimen shape and to find a specimen geometry which promotes failure at the hole. Failure initiation was predicted using the LaRC03 failure criterion [37]. Different specimen shapes were considered ranging from the butterfly specimen, inspired by the original Arcan tests [21], to lightly waisted specimens, to straight-sided specimens. The overall conclusion was that straight-sided specimens subjected to shear dominated load cases are prone to damage occurring at the top

right and bottom left corners of the specimen due to the high y-direction normal stresses/strains developing (see Fig. 7 (b)) and that the predicted probability of failure at the hole for lightly waisted specimens is improved. It is concluded that the lightly waisted specimen with a hole offers the best compromise with respect to promoting failure initiation at the hole across all laminate lay-ups and load cases. Pilot tests were carried out, which confirmed the findings of the FEA, hence the specimen shape as shown in Fig.4 was adopted.

Prior to bonding the end tabs, a large batch of specimens was water jet cut following the dimensions in Fig. 4 (a). Water jet cut tabs as shown in Fig 4. (c), made from 2 mm thick quasi-isotropic glass/epoxy circuit board material [38], were bonded to the carbon/epoxy using aerospace grade epoxy adhesive Araldite 2015 [39]. To facilitate the bonding process, slots were integrated into the specimen shape as shown in Fig. 4 (a) and (c). The tabs were aligned using M6 bolts as shown in Fig. 4 (e), ensuring an accurate alignment and bond line thickness. The alignment bolts were removed prior to testing.

The fibre orientation was defined with respect to the y-axis perpendicular to the waistline as shown in Fig. 4 (e) of the undeformed specimen, such that the surface ply was orientated at an angle of $\theta = +45^\circ$ for Laminates 1 and 2 and at $\theta = +22.5^\circ$ for Laminate 3. After water jet cutting, the central hole was drilled using a tungsten carbide drill bit on a pillar drill. Due to the limited amount of material supplied in combination with the large number of tests needed for multiaxial testing, the specimens were pre-screened using X-ray Computed Tomography (CT) with a voxel resolution of 30 μm . Based on visual inspection of the scans, the best specimens with the least manufacturing induced defects (e.g. inter/intra ply voids from lamination process or damage to edges due to the water jet cutting and drilling of holes) were selected for testing, to reduce the expected experimental scatter and thus justifying reduced numbers of test specimens per load and laminate configuration.

To improve the precision of the DIC measurements, an attempt was made to remove the peel ply pattern on the specimen surface which can adversely influence the correlation algorithm. Both sides of Laminate 2 specimens were therefore carefully sanded, but the attempt was stopped upon realisation that it is impossible to remove the peel ply pattern completely without

damaging the fibres of the surface plies. The surface plies of Laminate 2 specimens are therefore thinner than the rest of the plies. The total laminate thickness, t_{lam} , variation is reported in Table 2 as measured using a micrometre at three locations along the gauge section.

4 Load-extension curves derived from DIC based biaxial extensometer measurements

Load-extension curves provide a direct means of assessing the specimen load and failure response. In biaxial experiments such as in the MAF experiment, the test machine extension is only of limited use because the combined tension/compression and shear deformation is not separated. Furthermore, the test machine extension measurement is affected by the compliance of the test machine and additionally of the MAF assembly, which varies for the different loading angles, α , thus making direct comparisons between test cases difficult. Therefore, an alternative method of measurement of the specimen deformation is required that decouples the tension/compression and shear responses, and further is not affected by the compliance of the test set-up. In the following, a DIC based biaxial extensometer which overcomes these limitations is described. The derived load-extension curves are then used in Section 5 to discuss the load and failure response of the tested laminates.

Fig. 5 illustrates the principle of the biaxial extensometer based on DIC measurements. Vertical, v , and horizontal, u , displacements are extracted from the corresponding displacement fields near the top and bottom edges of the specimen averaged within 2 mm x 2 mm reference areas (red squares in Fig. 5 (a)). The positions of the reference areas are defined with respect to the centre of the hole, which is also the spatial origin of the DIC data. Thereby, three separate load-extension curves are derived on the left, on the centreline and on the right of the specimen as shown in Fig. 5 (a). The potential of exploiting the full field data and of deriving several load-extension curves is a further advantage of the DIC based extensometer, which allows a more detailed assessment of the specimen deformation in comparison to a conventional extensometer which only provides an averaged deformation measurement.

The extracted displacements u and v at the top and bottom edges, denoted by the superscript ‘top’ and ‘btm’, respectively, are then used to derive the vertical extension (normal response) and the horizontal extension (shear response) as follows:

$$\begin{aligned}\Delta v_i &= v_i^{top} - v_i^{btm} \\ \Delta u_i &= u_i^{top} - u_i^{btm}\end{aligned}\tag{1}$$

where the subscript i denotes the horizontal position of the virtual extensometer, i.e. left, centre and right, as illustrated in Fig. 5 (a). The extensions are then used to plot the normal and shear load-extension curves; a typical example is shown in Fig. 5 (b).

To extract the extensions from the DIC displacement fields, the global x,y,z position coordinates and the corresponding u , v , w displacements were exported from the DIC software and post-processed with a purpose-written Python code. Firstly, the position and displacement vectors were transformed so that the origin of the data corresponded to the centre of the hole (via translation transformation) and that the global z-axis was perpendicular to the specimen’s surface, while the top and bottom edges were parallel to the global x- axis (via rotation transformation). In the next step, the transformed data, highlighted grey in Fig. 6 (a), was interpolated on a grid of 0.05 mm x 0.05 mm indicated by black dots in Fig. 6 (a) [40].

To use DIC as a biaxial extensometer as described above, it is essential that the kinematics of the MAF are accounted for during data post-processing. As load is applied, an in-plane rigid body rotation of the specimen occurs, so a specimen reference $x^k y^k$ - coordinate system is defined that rotates with the specimen (see Figure 6 (b)), where k denotes the corresponding load step. At P^0 (zero loading), the specimen reference coordinate system, i.e. the $x^0 y^0$ - coordinate system, is equivalent to the global xy-coordinate system. The rigid body rotation angle upon loading is denoted ϕ^k in Fig. 6 (b) and is dependent on the applied load. The rigid body rotation angle is derived by fitting a straight line to the v - displacements along a line near to the bottom edge of the specimen shown in cyan in Fig. 6 (a). Based on the slope of the fitted line, a^k , the rigid rotation angle, ϕ^k , can be determined as shown in Fig. 6 (b) for every load step, k . Corrected displacement fields in the specimen reference $x^k y^k$ - frame were then obtained by

superposition of the rigid body rotation fields corresponding to a rigid rotation, ϕ^k , and the measured fields. The corrected fields are then used to derive the load-extension curves as shown in Fig. 5 (b).

5 Failure initiation and evolution

The MAF/DIC approach was used to investigate the three laminate configurations (see Fig. 1) subjected to tension ($\alpha = 0^\circ$), combined tension-shear ($\alpha = 15^\circ, 45^\circ$), shear ($\alpha = 90^\circ$), compression-shear ($\alpha = 135^\circ, 165^\circ$) and compression ($\alpha = 180^\circ$). The detailed testing protocol is attached in Appendix A. Fig. 7 shows the complex strain fields induced in specimens loaded in tension ($\alpha = 0^\circ$) and shear ($\alpha = 90^\circ$), obtained using DIC. In the linear elastic part of the load response, strain fields for combined load cases are simply linear superpositions of the strain fields shown in Fig. 7. Failure modes and locations discussed later can in some cases be attributed to the strain concentrations seen in Fig. 7. Further, the fields can be used to validate model predictions for the elastic material response before failure initiation.

Fig. 7 (a) shows that in tension loaded specimens, vertical tensile normal strain concentrations ε_{yy} develop on both sides of the hole, while shear strain concentrations γ_{yx} are observed as a radial pattern around the hole. The strain fields agree well with similar data in the literature for open-hole tensile tests [41]. Notably γ_{yx} and ε_{xx} strains also develop at the curved specimen edges. Fig. 7 (b) shows the development of high γ_{yx} shear strain concentrations in a radial pattern around the hole, while high compressive ε_{yy} and ε_{xx} normal strains are observed around the hole as well. Notably ε_{yy} strains also develop in the four corners of the specimen at the curved edges.

Based on the DIC results, two distinct failure events were observed across the load and lay-up configurations tested. Matrix cracks in the surface plies ($+45^\circ$ for Laminates 1 and 2, $+22.5^\circ$ for Laminate 3) can accurately be located based on the maximum principal normal strain fields, ε_{\max} , as shown in Fig. 8. Here the maximum principal strain is used because it is invariant to coordinate system transformation, thus simplifying comparison between specimens and with model predictions.

A second failure event can be determined from the out-of-plane displacement maps shown in Fig. 9, where local out-of-plane displacement changes indicate the occurrence of sub-surface damage. The local surface elevation indicates the formation of a displacement discontinuity in the through-thickness direction. While the associated initial damage mode cannot be clearly determined, it is confirmed by visual inspection that the out-of-plane displacement gradients result in the initiation of delamination (cracks at the interfaces of the plies). This can be seen through DIC camera 2 (see Fig. 3), through which the hole and the side edges of the specimen can be observed.

In load cases with a dominant shear component, high out-of-plane displacement gradients in the vicinity of the hole aligned with the $+45^\circ$ fibre direction are observed as shown for example in Fig. 9 (a) for Laminate 1 loaded in shear. Delamination cracks open further in shear and compression dominated load cases, which enhances their signature in the out-of-plane displacement plots. In the out-of-plane displacement maps for the tensile load cases shown in Fig. 9 (b), delaminated areas can also be identified: The dark red areas are clearly associated with edge/hole induced delamination failure, verified by visual inspection of the specimen edges through DIC camera 2 (see Fig. 3). A less pronounced change in the out-of-plane displacement is observed at the top and the bottom of the hole. Based on similar experimental data in the literature [42], this indicates delamination in the $0^\circ/-45^\circ$ ply interface between the two fibre splits typically occurring in the 0° plies of quasi-isotropic OHT specimens at both sides of the hole.

The main failure events are chronologically identified in the load-extension plots in Fig. 10 to 14 for specimens loaded in tension ($\alpha = 0^\circ$), tension-shear ($\alpha = 45^\circ$), shear ($\alpha = 90^\circ$), compression-shear ($\alpha = 135^\circ$) and compression ($\alpha = 180^\circ$), respectively. All load-extension curves, as given in Figs. 10 to 14, display linear behaviour for most part of the load response regardless of the applied combined load case. Only the shear responses for all load cases display nonlinear behaviour close to the maximum load. It is also noted that all laminates show the same compliance within the linear elastic load regime, confirming that the homogenised elastic properties of the three laminate configurations are equivalent. Most of the load-extension curves

obtained for a given specimen at the left, centre and right are in close agreement. However, for some cases, the normal load extension curves ($P - \Delta v_i$) obtained at the different horizontal locations deviate slightly (see e.g. Laminate 2 in Fig. 11). This indicates that damage does not necessarily occur simultaneously on both sides of the specimens but that one side cracks first, leading to stiffness reduction on one side of the specimen. This may be due to material variability or due to a slightly asymmetrical load introduction to the specimen. Further, it is observed that failure events detectable in the DIC fields are not necessarily reflected as a load drop in the load-extension plots, nor can the failure events be easily detected by visual inspection alone. This makes DIC an effective identification tool to characterise damage events that otherwise would be overseen. However, it should be noted that DIC is a surface-based technique, and although some internal damage events or internal nonlinearities as in [43] may be observed on the surface, not all internal failure events are detectable on the specimen surfaces. Detecting such damage events would require the use of e.g. X-ray CT [18], which is beyond the scope of this paper. Nevertheless, the obtained data is useful to visualise failure locations and governing failure mechanisms of the laminate which provide means to validate failure models. By assessing initial failure events across all load and lay-up configurations, the following can be concluded:

- For tensile dominated load cases ($\alpha = 0^\circ, 15^\circ$) the first detectable failure events in all laminates are inter-fibre matrix cracks in the surface plies starting at the hole and the edges (Fig. 10). The cracks initiating at the hole can clearly be attributed to the high tensile vertical normal strain concentrations shown in Fig. 7 (a).
- For tension-shear ($\alpha = 45^\circ$) loading, the first failure initiation in Laminates 1 and 2 are inter-fibre matrix cracks on the surface whereas Laminate 3 delaminates at the hole (Fig. 11).
- For shear ($\alpha = 90^\circ$) and combined compression-shear ($\alpha = 135^\circ, 165^\circ$) loading, failure initiates in all laminates at the hole (Fig. 12 and 13). Damage initiation is firstly observed in the out-of-plane displacement maps and results in delamination failure at the hole. The

damaged region can clearly be attributed to the high vertical compressive normal strain concentration above and below the hole shown in Fig. 7 (b).

- Failure in compression ($\alpha = 180^\circ$) occurs suddenly and without any notable prior failure events on the surface of the specimen (Fig. 14).

6 Ultimate multiaxial open-hole specimen strength

To compare the ultimate multiaxial open-hole specimen strength among the three laminates with respect to the different load cases, tension/compression-shear failure envelopes were derived. Therefore, the normal, N_y^{ult} , and shear, N_{yx}^{ult} , component of the ultimate failure load, P^{ult} , were obtained using the corresponding loading angle, α , as illustrated in Fig. 15, as follows:

$$N_y^{ult} = P^{ult} \cos(\alpha) \quad (2)$$

$$N_{yx}^{ult} = P^{ult} \sin(\alpha) \quad (3)$$

P^{ult} is expected to be influenced by the specimen shape and hole size, which is also intrinsic to uniaxial open-hole tests [9], [10], and it has been shown in Section 5 that damage has not in all cases initiated at the hole. The measured ultimate failure load (or average failure stress) is therefore best regarded as the failure load (or strength) of the specimen. Furthermore, mean representative stress based ultimate failure envelopes ($\overline{\sigma_{yy}^{ult}}$ - $\overline{\tau_{yx}^{ult}}$) were also defined as follows:

$$\overline{\sigma_{yy}^{ult}} = \frac{N_y^{ult}}{w_{net} t_{lam}} \quad (4)$$

$$\overline{\tau_{yx}^{ult}} = \frac{N_{yx}^{ult}}{w_{net} t_{lam}} \quad (5)$$

where w_{net} and t_{lam} are the measured net width and thickness of the gauge cross section, respectively. Note that the mean stresses do not represent the actual stresses which govern failure, but instead serve as a convenient averaged (across specimen cross section) quantity to compare the performance of all laminates for different combined loading in this study.

The ultimate failure loads, P^{ult} , as measured by the load cell of the test machine and corrected for the weight of the MAF and the balance system (see Fig. 3) are reported in Table 3 for all specimens. For the case of compressively loaded specimens ($\alpha = 180^\circ$), an additional failure load is reported which can be associated with the onset of laminate crushing which is characterised by the start of regular small load drops in the test machine load-displacement curves.

Table 3 shows that all laminates are strongest when loaded in tension ($\alpha = 0^\circ$), and that the addition of shear reduces the maximum load carrying capability. The ultimate failure load increases again when compressive loading is applied and reaches about half of the ultimate tensile failure load in compression ($\alpha = 180^\circ$). Fig. 16 shows the tension/compression-shear failure envelopes derived using Equations (2) to (5) based on the ultimate failure loads in Table 3 in load space (a) and stress space (b), respectively.

Fig. 16 reveals a strong effect of ply thickness on the load carrying capability when the specimens are subjected to tension-shear loading. The effect is most pronounced at $\alpha = 15^\circ$, where specimens made from ‘thin’ ply Laminates 2 and 3 carry up to 150% of the load carried by specimens made of ‘thick’ ply Laminate 1. The ply thickness effect in combined tension-shear is therefore also considerably greater than for tensile loaded specimens. The observed behaviour for tension-shear loading can be related to the in-situ strength effect that states that matrix cracking in UD plies is delayed in ‘thin’ plies compared to ‘thick’ plies [2], as well as to the higher delamination onset stresses in the ‘thin’ plies [6]. Moreover, matrix cracking and delamination failure in open-hole tests are interacting, thus suppressing matrix cracking in the ‘thin’ plies will also delay the onset of delamination [11] and subsequent fibre failure, which both govern the ultimate strength.

In contrast, the effect of ply thickness on the open-hole specimen strength is not evident for compression-shear loading. The in-situ effect on the transverse compressive strength is smaller than on the transverse tensile strength [44], resulting in similar crack initiation stresses for the ‘thin’ and ‘thick’ ply laminates loaded in the compressive loading regimes. Furthermore, the load-carrying capability in compression-shear of all laminates is limited by the relatively low

compressive UD fibre strength. Thus, delaying the onset of matrix cracking and delamination has not such a significant effect on the ultimate open-hole specimen strength in compressive loading regimes as in the tensile loading regime where delamination dominates ultimate failure.

Furthermore, no significant effect of the relative fibre orientation angle (45° versus 22.5°) on the ultimate load carrying capability can be seen by comparing the load based failure envelopes in Fig 16 (a) of the ‘thin’ ply Laminates 2 and 3, with an average difference in failure load of only 1% between the laminates. However, based on the mean stress based failure envelope in Fig. 16 (b), Laminate 2 sustains on average 10% higher stresses than Laminate 3. This difference may at first glance indicate the existence of a minor effect of the relative ply orientation angle on the ultimate load carrying capability. However, because Laminate 2 is on average 10% thinner than Laminate 3 due to the sanded surface plies (as described previously), it cannot be concluded that this phenomenon is attributed to the ply orientation effect alone. Instead, it is more likely that the surface 45° ply has only a minor influence on the ultimate strength of the laminate. Hence, partial removal of the Laminate 2 surface plies does not significantly reduce the ultimate failure load of Laminate 2 as evidenced in Fig. 16 (a). However, it increases the derived mean stresses in Fig. 16 (b) due to the reduced overall laminate thickness. It can therefore be concluded that if an effect of the relative fibre orientation on the ultimate failure load does exist, it will be much smaller than the effect of ply thickness for the laminates and load cases investigated here.

Photographs of selected specimens after ultimate failure are presented in Table 4. Where the specimens have not fractured into two halves, schematics of the through-thickness crack paths are presented for clarity. It should be noted that, although some initial failure events can be distinguished (see Figs. 10- 14), a cascade of various interacting failure events (transverse matrix cracks, fibre breaks, delamination) happen suddenly and within a fraction of a second. This means that the ultimate failure pattern is influenced by highly dynamic events inducing a considerable degree of variability in the patterns observed. Nevertheless, from visual inspection, the following observations can be made that will facilitate the validation of predictive models:

- For tensile dominated load cases ($\alpha = 0^\circ, 15^\circ$), all specimens fail in the typical open-hole tensile test pattern as reported in the literature [9]. All specimens break in two halves, indicating that final failure involves complete fracture of the 0° plies and in the case of Laminate 3 also the $\pm 22.5^\circ$ plies.
- For combined tension-shear loading ($\alpha = 45^\circ$), the specimens no longer fail in the typical open-hole tensile specimen pattern [9]. Instead, macroscopic fracture planes (i.e. areas of major damage accumulation in the form of matrix cracks, delamination and fibre failure) run from the bottom left corner through the hole to the top right corner, where both corner areas are largely delaminated. The opposite corners instead show only little damage. Specimens of Laminate 2 break in two halves while specimens of Laminate 1 and 3 do not disintegrate completely but develop a series of through-thickness cracks forming effectively a wedge centred by the mid 0° plies.
- For shear and moderate combined compression-shear loading ($\alpha = 90^\circ - 135^\circ$), all specimens exhibit a macroscopic fracture plane running diagonally from bottom left to top right corners accompanied by large delamination in the same corners, while the opposite corners show little damage. For Laminates 1 and 3 a through-thickness wedge shaped crack path is evident, while Laminate 2 shows a dispersed crack pattern.
- For compressive load cases ($\alpha = 165^\circ - 180^\circ$), the fracture planes align approximately with the minimum gauge section. In the through-thickness view, the cracks are dispersed, and the plies are crushed accompanied by matrix cracking, fibre breaks and delamination.

7 Conclusions and future work

A novel experimental procedure based on a new Modified Arcan Fixture (MAF), stereo Digital Image Correlation (DIC) and a lightly waisted open-hole specimen has been devised to investigate multidirectional laminates subjected to combined tension/compression and shear loading. The new MAF has enabled the characterisation of multidirectional composite laminates subjected to both combined tension-shear and compression-shear loading, which has not been possible before. Using the developed experimental procedure, three quasi-isotropic

carbon/epoxy laminates were tested to investigate the effect of ply thickness and relative fibre orientation angles on the failure initiation and ultimate multi-axial open-hole specimen strength of multidirectional laminates.

Based on the DIC measurements, two macroscopic failure events were distinguished, i.e. matrix cracking of the surface plies and delamination at the hole. For specimens loaded in tension and combined tension-shear, initial failure events (matrix cracking in the surface ply) occurred simultaneously at the hole and the edges, while for the shear, combined compression-shear and compression load cases, the first failure events occurred at the hole. Load-extension curves were constructed based on the full-field displacement maps, which enabled the visualisation of the combined tension/compression-shear deformation and failure evolution. The experimental data obtained showed laminate lay-up effects on failure evolution and ultimate failure. Moreover, it revealed significant dependencies of the magnitude of the laminate lay-up effect on the applied combined load case. For combined tension-shear loading, ply thickness has a strong effect on the ultimate specimen failure strength, where the ‘thin’ ply specimens were up to 150 % stronger than the ‘thick’ ply specimens. However, for combined compression-shear loading no significant ply thickness effect was observed. Furthermore, no significant effect of the relative fibre orientation angle on the ultimate strength was observed regardless of the combined loading regime.

The overarching conclusion from the work in the paper impacts on the design of high-performance composite materials and structures, in that the use of laminates with thinner but increased numbers of plies may be preferential in areas of combined tension-shear loading, despite the increased manufacturing cost. However, for the material systems investigated, no significant benefit is apparent for using the ‘thin’ plies for laminates subjected predominantly to compression-shear loading. Moreover, according to the experiments conducted there is no significant gain of using non-standard fibre orientation angle laminates in terms of ultimate strength for the investigated load cases. However, further investigation is needed to ascertain if these findings are applicable for different hole sizes or stress raiser geometries, i.e. different specimen shapes.

The work conducted provides a definitive demonstration of the usefulness of the developed MAF/DIC procedure to study multidirectional composite laminates subjected to combined tension/compression-shear loading. Based on the promising test results, it is recommended for future work to investigate the possibility for an improved specimen design to encourage failure initiation at the hole to improve comparability of the multiaxial open-hole strength. Furthermore, the use of X-ray CT in combination with the MAF test is recommended for future work which would enable the clear identification of sub-surface damage events which could be correlated against surface-based observations.

Furthermore, the complex material behaviour captured in the MAF test results stemming from the various lay-up and load configurations investigated, makes the extracted high-fidelity experimental data well suited for the validation and development of novel numerical and analytical tools to predict failure in composite laminates. Thorough validation against challenging and high-fidelity experimental data, as successfully delivered by the research described in the paper, is crucially important to raise confidence in numerical tools for composite failure analysis. Future work will focus on assessing the agreement between the experimental observations presented in this paper, and numerical predictions made using the meso-scale FE modelling framework proposed in [29], with the aim of establishing its maturity and its readiness for industrial design and certification.

Acknowledgements

This work is supported by EPSRC under the Doctoral Training Grant 1801230 and through a Stanley Gray Fellowship granted to the lead author by the Institute of Marine Engineering, Science and Technology (IMarEST). The μ -VIS X-Ray Imaging Centre of the University of Southampton is acknowledged for providing the computed tomography facilities used in this study. The MAF/DIC approach described in the paper was developed and commissioned in the Testing and Structures Research Laboratory (TSRL) at the University of Southampton. The guidance of the TSRL Principal Experimental Officer Dr. Andy Robinson on various topics regarding experimental set-up and techniques is gratefully acknowledged.

References

- [1] P. P. Camanho and S. R. Hallett, Eds., *Numerical Modelling of Failure in Advanced Composite Materials*. Woodhead Publishing, 2015.
- [2] A. Parvizi, K. W. Garrett, and J. E. Bailey, “Constrained cracking in glass fibre-reinforced epoxy cross-ply laminates,” *J. Mater. Sci.*, vol. 13, no. 10, pp. 2131–2136, 1978.
- [3] D. L. Flagg, “Experimental determination of the in situ transverse lamina strength in graphite / epoxy laminates,” *J. Compos. Mater.*, vol. 16, pp. 103–116, 1982.
- [4] F. Chang and M. Chen, “The in situ ply shear strength distributions in graphite/epoxy laminated composites,” *J. Compos. Mater.*, vol. 21, pp. 708–733, 1986.
- [5] A. Arteiro, G. Catalanotti, A. R. Melro, P. Linde, and P. P. Camanho, “Micro-mechanical analysis of the effect of ply thickness on the transverse compressive strength of polymer composites,” *Compos. Part A Appl. Sci. Manuf.*, vol. 79, pp. 127–137, 2015.
- [6] W. Cui and M. R. Wisnom, “An experimental and analytical study of delamination of unidirectional specimens with cut central plies,” *J. Reinf. Plast. Compos. Plast.*, vol. 13, pp. 722–739, 1994.
- [7] G. J. Dvorak and N. Laws, “Analysis of progressive matrix cracking in composite laminates II. first ply failure,” *J. Compos. Mater.*, vol. 21, no. 4, pp. 309–329, 1987.
- [8] P. P. Camanho, C. G. Davila, S. T. Pinho, L. Iannucci, and P. Robinson, “Prediction of in situ strengths and matrix cracking in composites under transverse tension and in-plane shear,” *Compos. Part A Appl. Sci. Manuf.*, vol. 37, no. 2, pp. 165–176, 2006.
- [9] B. G. Green, M. R. Wisnom, and S. R. Hallett, “An experimental investigation into the tensile strength scaling of notched composites,” *Compos. Part A Appl. Sci. Manuf.*, vol. 38, no. 3, pp. 867–878, 2007.
- [10] S. R. Hallett, B. G. Green, W. G. Jiang, and M. R. Wisnom, “An experimental and numerical investigation into the damage mechanisms in notched composites,” *Compos. Part A Appl. Sci. Manuf.*, vol. 40, no. 5, pp. 613–624, 2009.

- [11] M. R. Wisnom and S. R. Hallett, "The role of delamination in strength, failure mechanism and hole size effect in open hole tensile tests on quasi-isotropic laminates," *Compos. Part A Appl. Sci. Manuf.*, vol. 40, no. 4, pp. 335–342, 2009.
- [12] M. J. Hinton and A. S. Kaddour, "The background to the second world-wide failure exercise," *J. Compos. Mater.*, vol. 46, no. 19–20, pp. 2283–2294, 2012.
- [13] U. Kureemun, M. Ridha, and T. Tay, "Biaxial tensile-compressive loading of unnotched and open-hole carbon epoxy crossply laminates," *J. Compos. Mater.*, vol. 49, no. 23, pp. 2817–2837, 2014.
- [14] K. W. Gan, S. R. Hallett, and M. R. Wisnom, "Measurement and modelling of interlaminar shear strength enhancement under moderate through-thickness compression," *Compos. Part A Appl. Sci. Manuf.*, vol. 49, pp. 18–25, 2013.
- [15] K. W. Gan, M. R. Wisnom, and S. R. Hallett, "Effect of high through-thickness compressive stress on fibre direction tensile strength of carbon/epoxy composite laminates," *Compos. Sci. Technol.*, vol. 90, pp. 1–8, 2014.
- [16] J. P. Boehler, S. Demmerle, and S. Koss, "A new direct biaxial testing machine for anisotropic materials," *Exp. Mech.*, vol. 34, no. 1, pp. 1–9, 1994.
- [17] A. Smits, D. Van Hemelrijck, T. P. Philippidis, and A. Cardon, "Design of a cruciform specimen for biaxial testing of fibre reinforced composite laminates," *Compos. Sci. Technol.*, vol. 66, no. 7–8, pp. 964–975, 2006.
- [18] J. L. Y. Tan, V. S. Deshpande, and N. A. Fleck, "Failure mechanisms of a notched CFRP laminate under multi-axial loading," *Compos. Part A Appl. Sci. Manuf.*, vol. 77, pp. 56–66, 2015.
- [19] K. W. Gan, T. Laux, S. T. Taher, J. M. Dulieu-Barton, and O. T. Thomsen, "A novel fixture for determining the tension/compression-shear failure envelope of multidirectional composite laminates," *Compos. Struct.*, vol. 184, pp. 662–673, 2018.
- [20] T. Laux, K. W. Gan, J. M. Dulieu-Barton, and O. T. Thomsen, "A simple nonlinear constitutive model based on non-associative plasticity for UD composites: Development and calibration using a Modified Arcan Fixture," *Int. J. Solids Struct.*, vol. 162, pp. 135–

- 147, 2019.
- [21] M. Arcan, Z. Hashin, and A. Voloshin, “A method to produce uniform plane-stress states with applications to fiber-reinforced materials,” *Exp. Mech.*, vol. 18, no. 4, pp. 141–146, 1978.
- [22] J. L. Y. Tan, V. S. Deshpande, and N. A. Fleck, “The effect of laminate lay-up on the multi-axial notched strength of CFRP panels: Simulation versus experiment,” *Eur. J. Mech. A/Solids*, vol. 66, pp. 309–321, 2017.
- [23] I. M. Daniel and O. Ishai, *Engineering mechanics of composite materials*. Oxford University Press, 2005.
- [24] P. P. Camanho, P. Maimí, and C. G. Dávila, “Prediction of size effects in notched laminates using continuum damage mechanics,” *Compos. Sci. Technol.*, vol. 67, no. 13, pp. 2715–2727, 2007.
- [25] E. Abisset, F. Daghia, and P. Ladevze, “On the validation of a damage mesomodel for laminated composites by means of open-hole tensile tests on quasi-isotropic laminates,” *Compos. Part A Appl. Sci. Manuf.*, vol. 42, no. 10, pp. 1515–1524, 2011.
- [26] R. Higuchi, T. Okabe, and T. Nagashima, “Numerical simulation of progressive damage and failure in composite laminates using XFEM/CZM coupled approach,” *Compos. Part A Appl. Sci. Manuf.*, vol. 95, pp. 197–207, 2017.
- [27] O. Falcó, R. L. Ávila, B. Tijs, and C. S. Lopes, “Modelling and simulation methodology for unidirectional composite laminates in a Virtual Test Lab framework,” *Compos. Struct.*, vol. 190, pp. 137–159, 2018.
- [28] S. Mukhopadhyay and S. R. Hallett, “A directed continuum damage mechanics method for modelling composite matrix cracks,” *Compos. Sci. Technol.*, vol. 176, pp. 1–8, 2019.
- [29] C. Furtado, G. Catalanotti, A. Arteiro, P. J. Gray, B. L. Wardle, and P. P. Camanho, “Simulation of failure in laminated polymer composites: Building-block validation,” *Compos. Structures*, vol. 226, 2019.
- [30] S. T. Taher, O. T. Thomsen, J. M. Dulieu-Barton, and S. Zhang, “Determination of mechanical properties of PVC foam using a modified Arcan fixture,” *Compos. Part A*

- Appl. Sci. Manuf.*, vol. 43, no. 10, pp. 1698–1708, 2012.
- [31] Verein Deutscher Ingenieure (VDI), “VDI 2230 Systematische Berechnung hochbeanspruchter Schraubenverbindungen - Zylindrische Einschraubenverbindungen,” 2003.
- [32] “BS EN ISO 898-1. 2009. Mechanical properties of fasteners made of carbon steel and alloy steel, Part 1: Bolts, screws and studs with specified property classes - Coarse thread and fine pitch thread.” BSI, 2009.
- [33] V. J. Muhs D., Wittel H., Becker M., Jannasch D., *Bolzen-, Stiftverbindungen, Sicherungselemente. In: Roloff/Matek Maschinenelemente Formelsammlung.* Wiesbaden, 2003.
- [34] E. M. C. Jones and M. A. Iadicola, *A good practices guide for digital image correlation.* 2018.
- [35] S. R. Hallett, B. G. Green, W. J. Kin, H. Cheung, and M. R. Wisnom, “The open hole tensile test : a challenge for virtual testing of composites,” *Int. J. Fract.*, vol. 158, pp. 169–181, 2009.
- [36] Dassault System, “Abaqus 6.14 Documentation.” 2017.
- [37] C. G. Dávila, P. P. Camanho, and C. A. Rose, “Failure criteria for FRP laminates,” *J. Compos. Mater.*, vol. 39, no. 4, pp. 323–345, 2005.
- [38] Aquarius Plastics, “TUFNOL Rods, Sheets & Tubes.” [Online]. Available: <https://www.aquariusplastics.co.uk/>. [Accessed: 07-May-2019].
- [39] Huntsman, “Araldite 2000+ Adhesives Data sheet.” [Online]. Available: http://www.huntsman.com/advanced_materials/Media Library/global/files/US 2000%2B Adhesives Selector Guide for Bonding_Assembly_Repair_Araldite.pdf. [Accessed: 07-May-2019].
- [40] E. Jones, T. Oliphant, and P. Peterson, “SciPy Open source scientific tools for Python.” 2001.
- [41] F. Pierron, B. Green, and M. R. Wisnom, “Full-field assessment of the damage process of lamianted composite open-hole tensile speciemns. Part I: Methodology,” *Compos.*

- Part A Appl. Sci. Manuf.*, vol. 38, pp. 2307–2320, 2007.
- [42] O. J. Nixon-Pearson, S. R. Hallett, P. J. Withers, and J. Rouse, “Damage development in open-hole composite specimens in fatigue. Part 1: Experimental investigation,” *Compos. Struct.*, vol. 106, pp. 882–889, 2013.
- [43] F. Pierron, B. Green, M. R. Wisnom, and S. R. Hallett, “Full-field assessment of the damage process of laminated composite open-hole tensile specimens. Part II: Experimental results,” *Compos. Part A Appl. Sci. Manuf.*, vol. 38, pp. 2321–2332, 2007.
- [44] A. Arteiro, G. Catalanotti, J. Reinoso, P. Linde, and P. P. Camanho, “Simulation of the mechanical response of thin-ply composites: from computational micro-mechanics to structural analysis,” *Arch. Comput. Methods Eng.*, vol. 26, pp. 1445–1487, 2019.
- [45] LaVision, “DaVis 10.0 Software: Product Manual.” Göttingen, 2018.

Appendix A: Testing protocol

The uniaxial tension tests ($\alpha = 0^\circ$) of Laminates 2 and 3 were conducted on an Instron Schenck 630 kN servo-hydraulic universal test machine, whereas all other tests were conducted on an Instron 8502 100 kN servo-hydraulic test machine. The following testing protocol for the MAF tests was strictly adhered to:

- 1) The MAF was connected to the test machine crosshead using an appropriate pair of loading holes by the aid of the pulleys as illustrated in Fig. 3.
- 2) The specimen was mounted and the clamping bolts (see Fig. 2 (b)) were torqued up to 75 Nm for $\alpha = 45^\circ - 180^\circ$ and up to 120 Nm for $\alpha = 0^\circ$ and 15° , respectively. A 3D printed jig was used to ensure accurate alignment of the specimen within the grips.
- 3) The balance weight system was installed to eliminate the spurious stresses/strain induced into the specimen by the weight of the MAF as shown in Fig. 3.
- 4) The load cell was balanced. Therefore, the load reading does not include the load carried by the specimen generated by the lower half of the MAF assembly and the connected balance weight. The load reading was therefore corrected in a post-processing step.
- 5) The MAF was connected to the test machine actuator at the bottom and was pre-tensioned to approximately $P = 0.1$ kN to take up initial slack in the MAF assembly.
- 6) Five static images were taken with the calibrated stereo DIC system of the undeformed specimen.
- 7) Image acquisition was started at a rate of 2 Hz. The specimen was loaded in displacement control (1 mm/min) until ultimate failure.

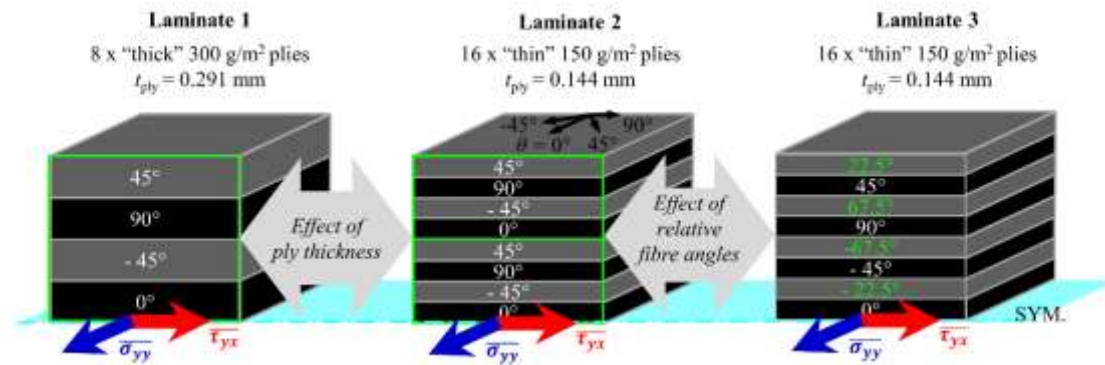


Fig 1. Quasi-isotropic carbon/epoxy laminates subjected to combined tension-shear and compression-shear loading.

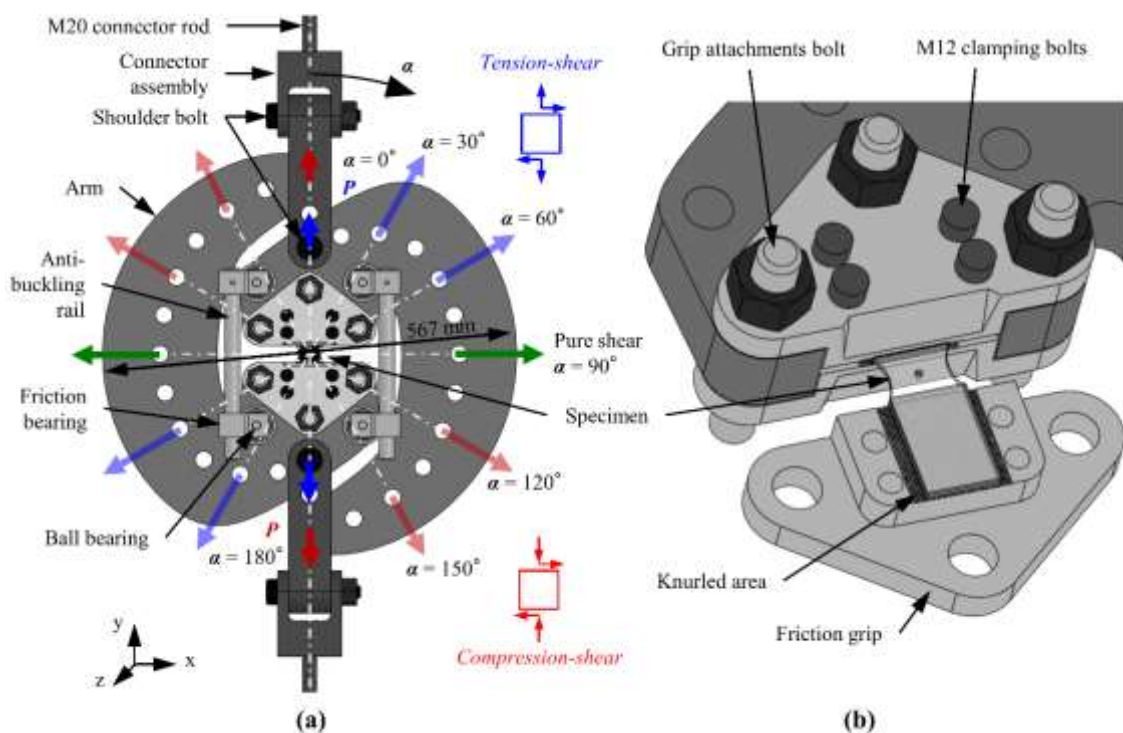


Fig 2. (a) The new Modified Arcan Fixture (MAF), with indication of how different combined tension/compression-shear loading can be induced in the specimen by the choice of the loading hole pair designated by the loading angle α , and (b) the re-designed specimen friction grip arrangement.

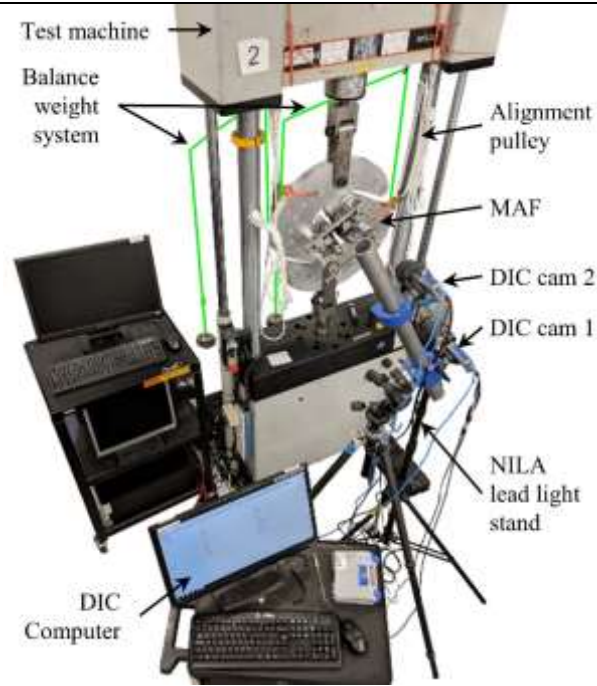


Fig. 3. Experimental set-up showing the MAF attached to universal test machine, the alignment pulleys, the balance weight system and the stereo Digital Image Correlation (DIC) system.

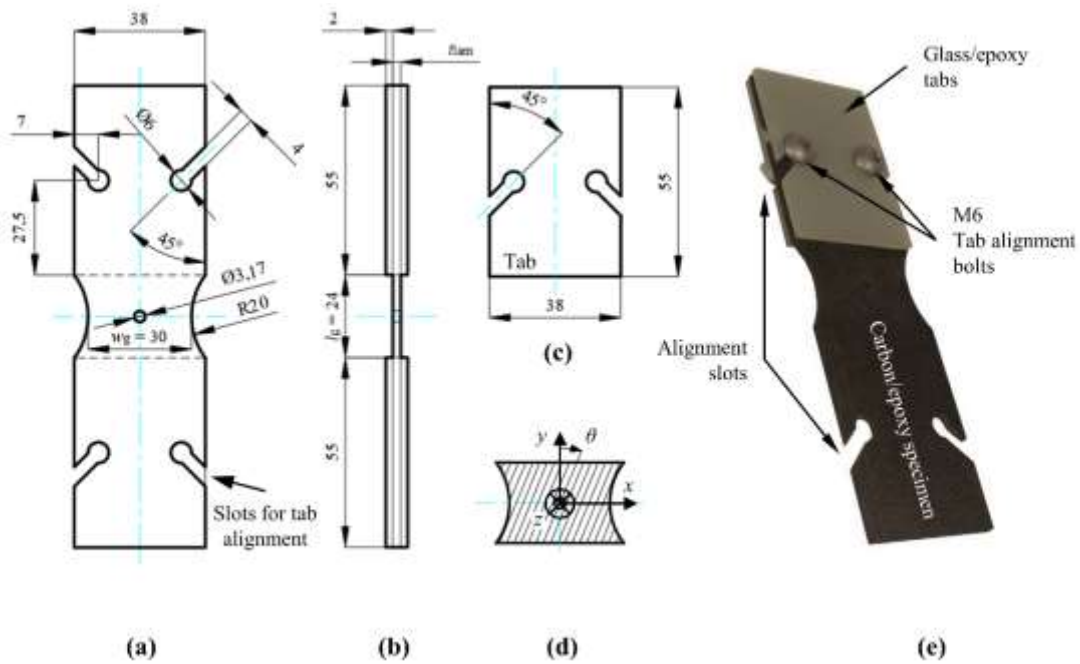


Fig 4. Specimen design; (a) in-plane view and (b) side view of the assembled specimen, (c) glass/epoxy tab, (d) definition of fibre orientation angle, θ , and (e) tabbing procedure using alignment slots and bolts. Dimensions given in mm.

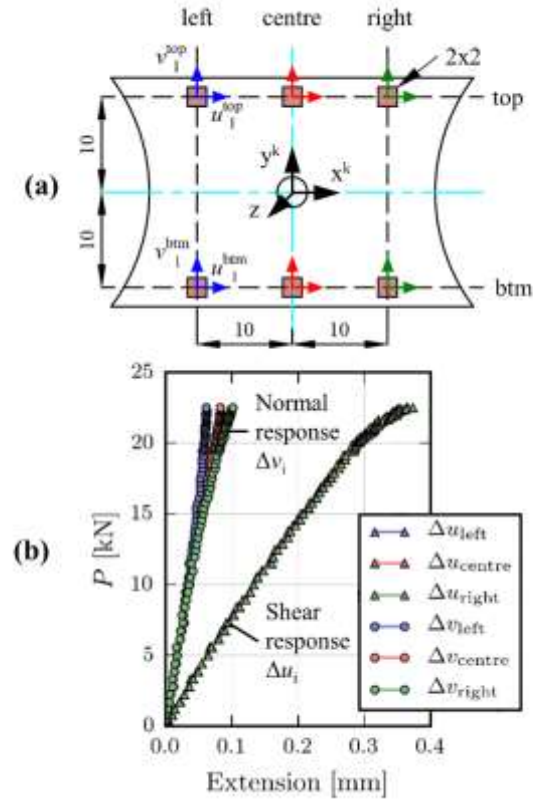


Fig. 5. Principle of the DIC based virtual extensometer: (a) Location of displacement extraction points and (b) example of derived load-extension curves for a Laminate 3 specimen loaded in combined tension- shear ($\alpha = 45^\circ$). Dimensions given in mm.

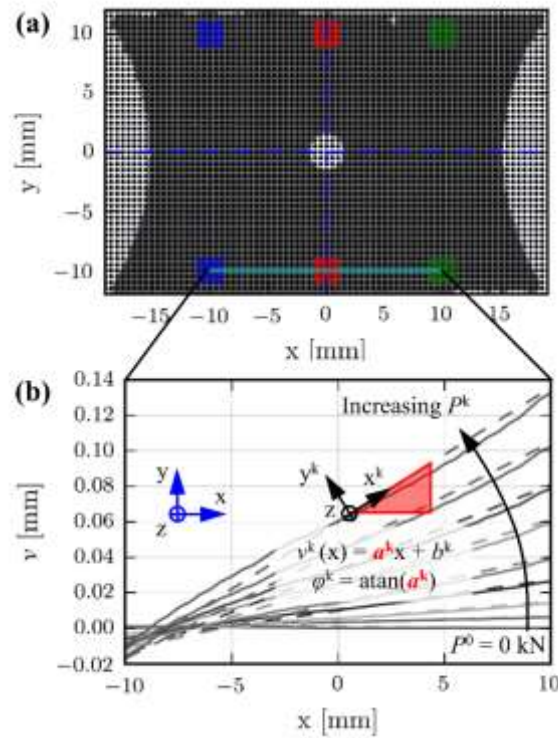


Fig. 6. Post-processing for virtual extensometer: (a) translating, rotating and interpolating scattered data on regular grid (matrix) and (b) procedure to characterise rigid body rotation.

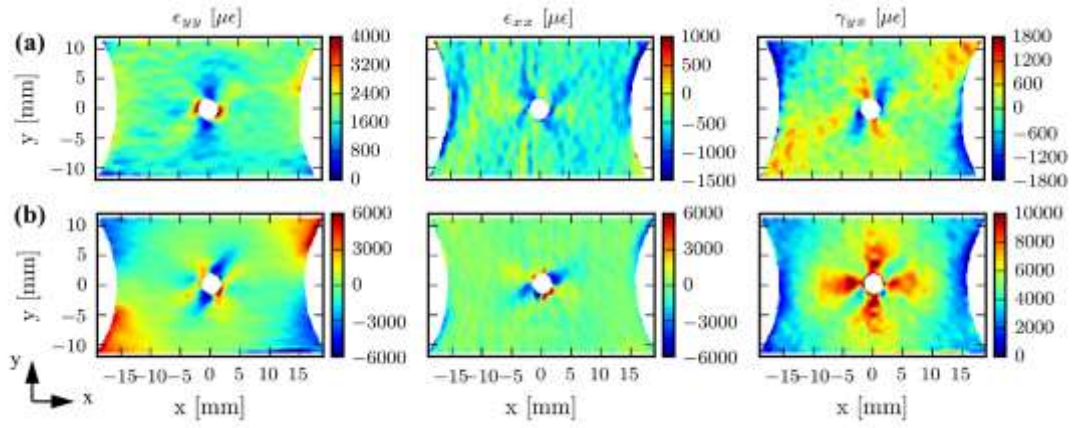


Fig. 7. Strain fields in open hole specimens at $P = 7.5$ kN before initiation of failure: (a) subjected to uniaxial tensile loading, and (b) subjected to shear loading.

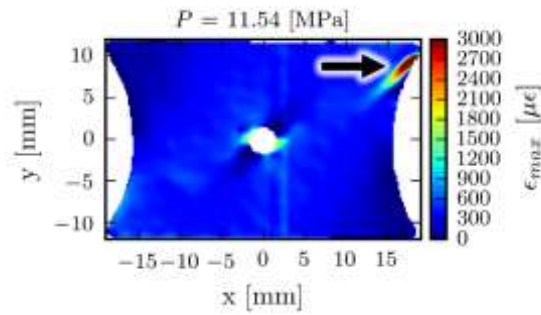


Fig. 8. Maximum principal normal strain field used to characterise transverse cracking of the surface plies. Example shown: Laminate 1 in tension-shear loading ($\alpha = 45^\circ$).

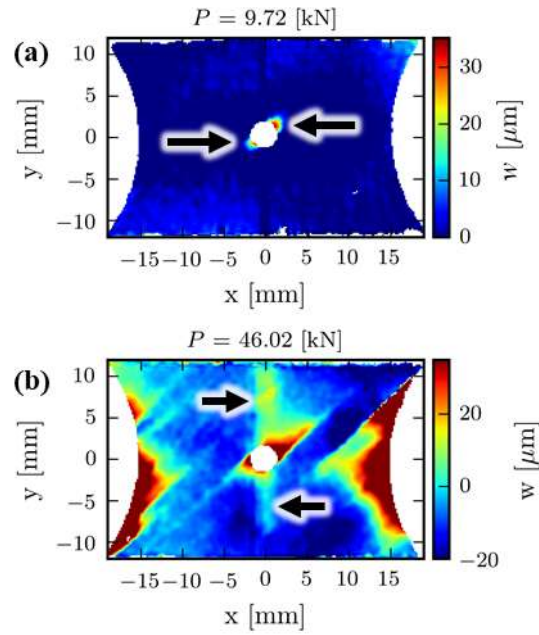


Fig. 9. Out-of-plane w -displacement field used to characterise delamination failure: (a) delamination damage at the notch for Laminate 1 loaded in shear ($\alpha = 90^\circ$) and (b) delamination at the notch and edges for Laminate 1 loaded in tension ($\alpha = 0^\circ$).

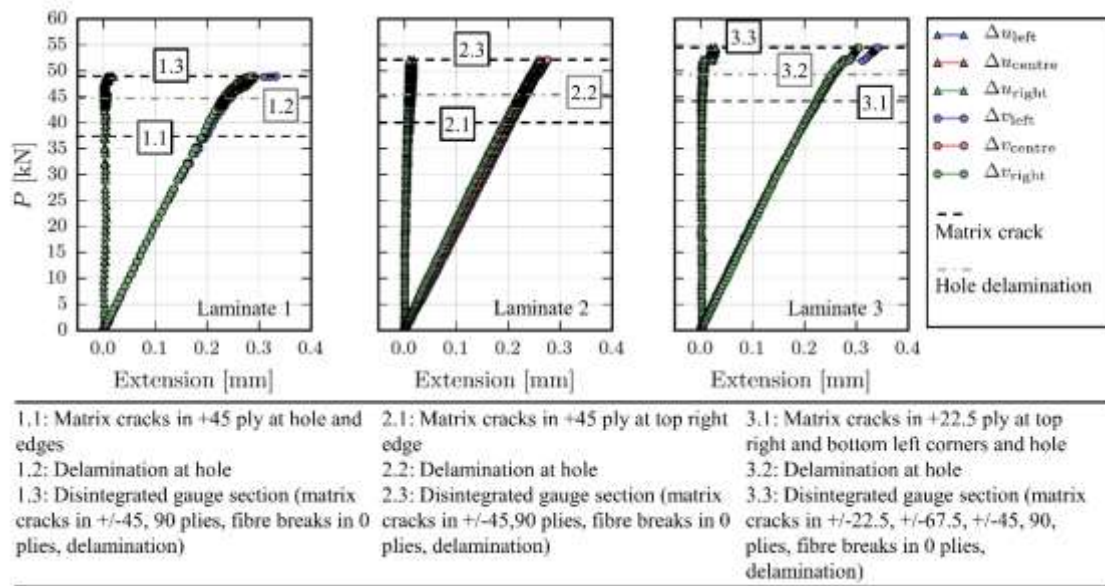


Fig. 10. Load-extension curves for Laminates 1 – 3 subjected to tension loading ($\alpha = 0^\circ$)

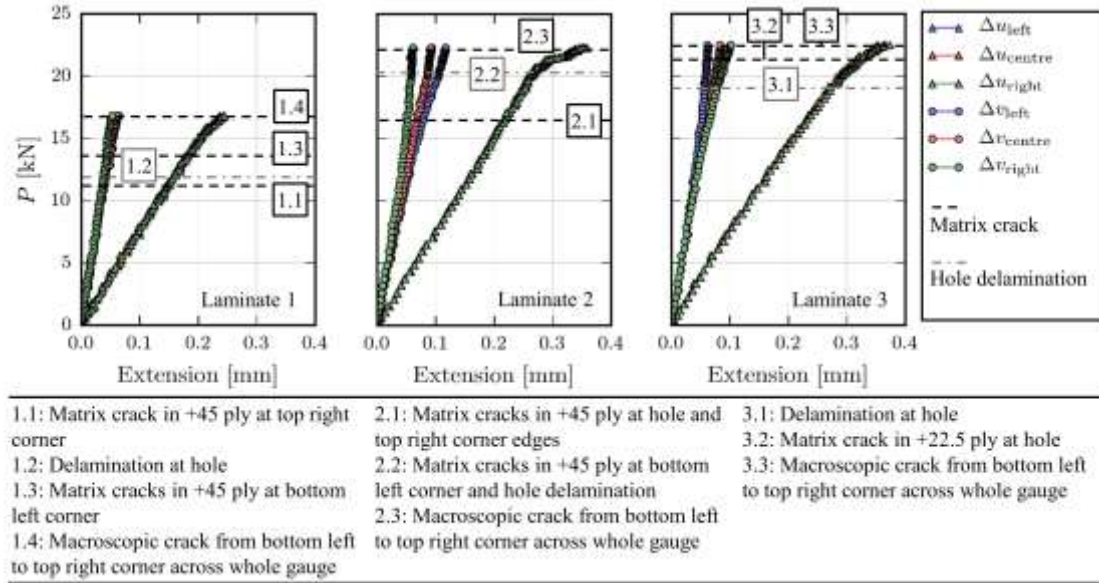


Fig. 11. Load-extension curves for Laminates 1 – 3 subjected to combined tension-shear loading ($\alpha = 45^\circ$).

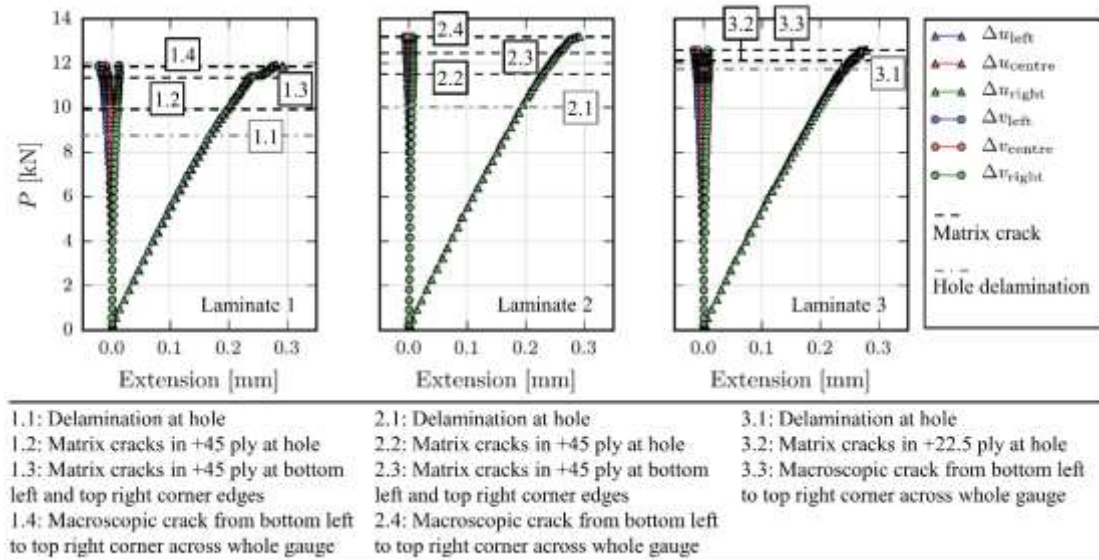


Fig. 12. Load-extension curves for Laminates 1 – 3 subjected to shear loading ($\alpha = 90^\circ$).

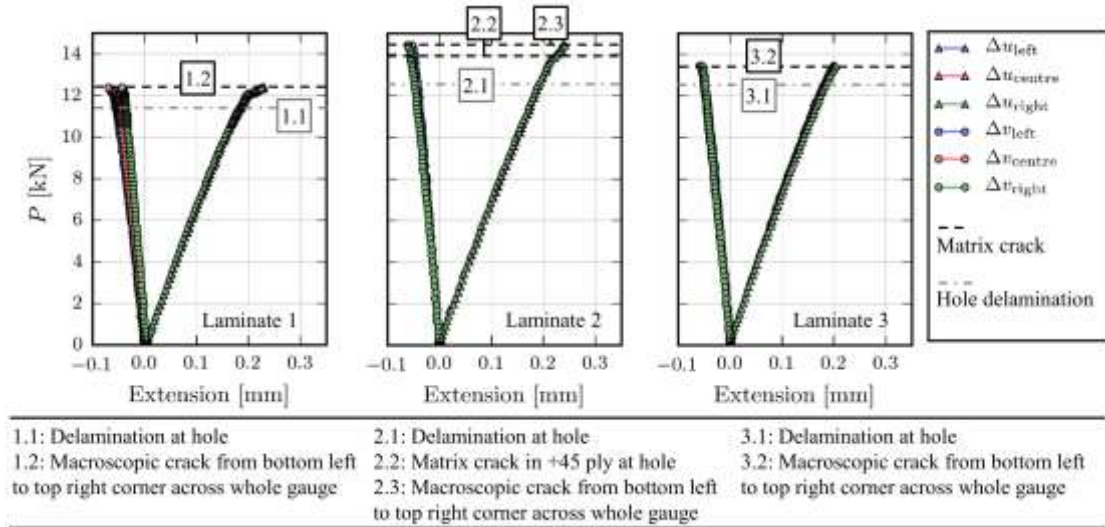


Fig. 13. Load-extension curves for Laminates 1 – 3 subjected to combined compression-shear loading ($\alpha = 135^\circ$).

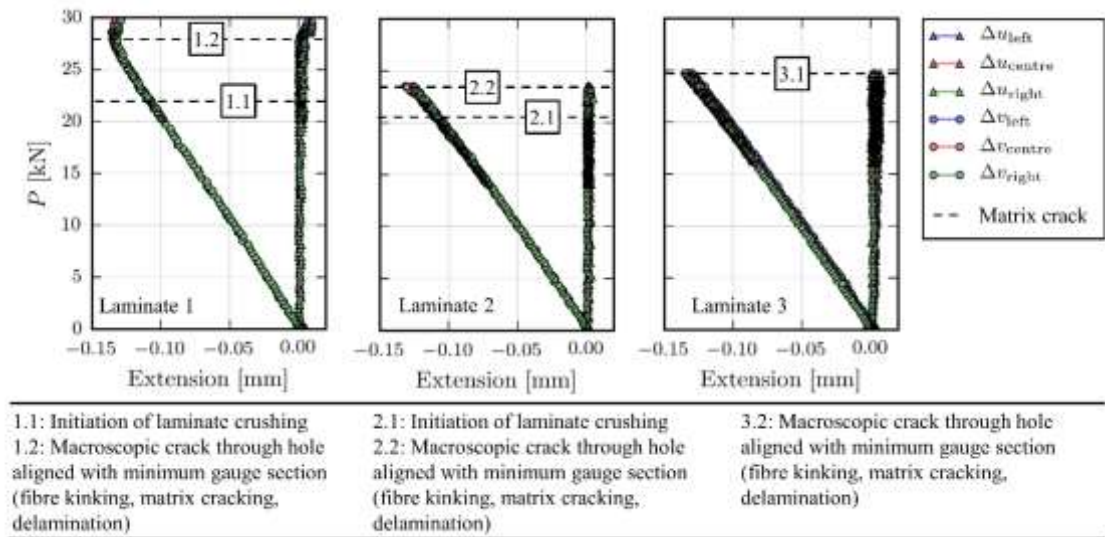


Fig. 14. Load-extension curves for Laminates 1 – 3 subjected to compression loading ($\alpha = 180^\circ$).

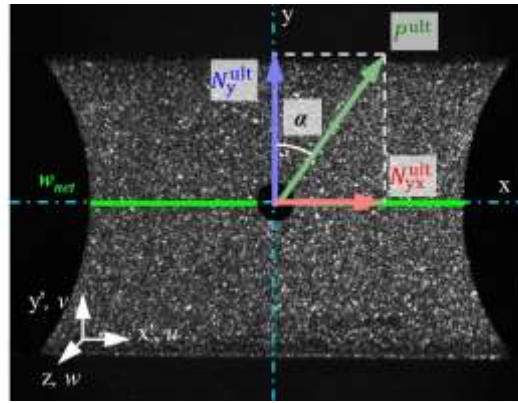


Fig. 15. View through DIC camera and definition of the representative combined tension/compression, N_y^{ult} , and shear, N_{yx}^{ult} , load case.

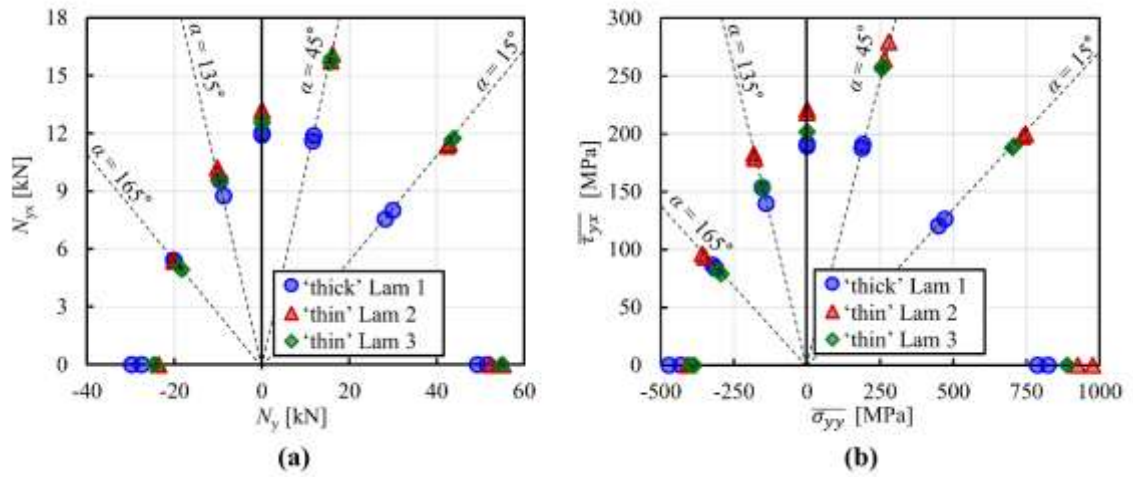


Fig. 16. Ultimate load carrying capability of the different laminate configurations and load cases: (a) measured load based failure envelope, (b) net cross section mean stress based failure envelope.

Table 1. DIC system specification, processing parameters and system performance.

| Hardware | |
|---|--|
| Cameras | 2 x Imager E-Lite 5M |
| Sensor and digitization | 2448 x 2050, 12 bit |
| Lens | Sigma 105 mm f/2.8 |
| Imaging distance [mm] / Stereo angle [deg] | ~ 500 / 20 |
| Lighting | 2 x NILA ZAILA LED Lights |
| Pixel resolution | ~ 50.62 pixel/mm |
| Field of View [mm] | ~ 40 x 48 |
| Analysis parameters | |
| Software | DaVis 10, LaVision [45] |
| Subset size [pixels] / Step size [pixels] | 51 / 10 |
| Shape function / Correlation Criterion | Quadratic / LSM |
| Spatial pre-filtering of displacements | Gaussian smoothing (3x3 kernel) |
| Strain tensor | Logarithmic |
| System performance | |
| Displacement noise floor [μm] | $u = 0.443$ / $v = 0.288$ / $w = 0.688$ |
| Strain noise floor [$\mu\text{m}/\text{m}$] | $\varepsilon_{xx} = 99$ / $\varepsilon_{yy} = 87$ / $\varepsilon_{yx} = 102$ |

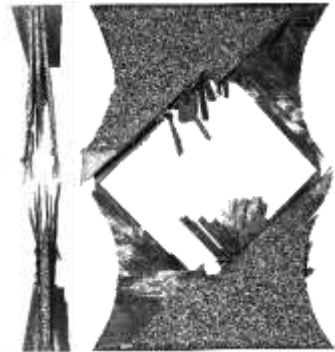
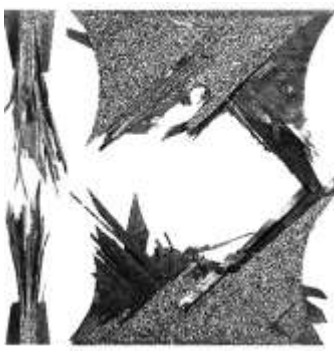


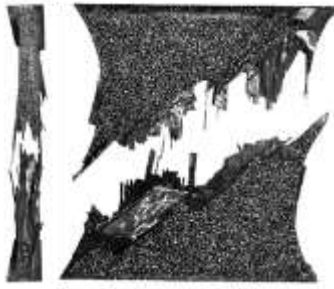
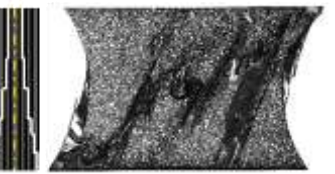


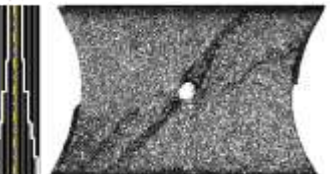



Table 2. Measured mean thicknesses of the specimens.

| | Laminate 1 | Laminate 2 | Laminate 3 |
|-----------------------|-------------------|-------------------|-------------------|
| t_{lam} [mm] | 2.326 | 2.133 | 2.301 |
| % COV | 1.29% | 2.71% | 1.08% |

Table 3. Ultimate failure loads, P^{ult} , sustained by each tested specimen.

| Load case | $\overline{\sigma_{yy}/\tau_{yx}}$ | Nr | Laminate 1 P^{ult} [kN] | Laminate 2 P^{ult} [kN] | Laminate 3 P^{ult} [kN] |
|--|------------------------------------|----|------------------------------|------------------------------|------------------------------|
| Tension $\alpha = 0^\circ$ | $+\infty$ | 1 | 51.58 | 55.16 | 54.84 |
| | | 2 | 49.33 | 52.29 | 55.06 |
| Tension-shear $\alpha = 15^\circ$ | 3.732 | 1 | 30.96 | 43.89 | 45.35 |
| | | 2 | 29.22 | 44.36 | 44.99 |
| Tension-shear $\alpha = 45^\circ$ | 1 | 1 | 16.80 | 22.29 | 22.51 |
| | | 2 | 16.41 | 22.79 | 22.18 |
| Shear $\alpha = 90^\circ$ | 0 | 1 | 12.02 | 13.21 | 12.62 |
| | | 2 | 11.92 | 13.18 | 12.53 |
| Compression-shear $\alpha = 135^\circ$ | -1 | 1 | 13.52 | 14.44 | 13.46 |
| | | 2 | 12.39 | 14.07 | 13.44 |
| Compression-shear $\alpha = 165^\circ$ | -3.732 | 1 | 20.95 | 20.71 | 19.01 |
| | | 2 | 20.71 | 20.86 | 19.60 |
| Compression $\alpha = 180^\circ$ * | $-\infty$ | 1 | 21.92 / 27.52 | 20.34 / 23.56 | - /24.75 |
| | | 2 | 20.92 / 29.77 | 21.42 / 23.77 | 23.52 / 24.51 |
| * Initiation of laminate crushing and maximum load sustained are reported if applicable. | | | | | |

Table 4. Selected specimens after ultimate failure. Crack paths are highlighted as white lines in through-thickness schematics in specimens that did not break in two halves.

| Laminate 1 | Laminate 2 | Laminate 3 |
|---|---|---|
| Tension dominated ($\alpha = 0^\circ - 15^\circ$) | | |
|  |  |  |
| Tension-shear ($\alpha = 45^\circ$) | | |
|  |  |  |
| Shear and shear with moderate compression ($\alpha = 90^\circ - 135^\circ$) | | |
|  |  |  |
| Compression dominated ($\alpha = 165^\circ - 180^\circ$) | | |
|  |  |  |